Check for updates

ADVANCED MATERIALS
www.advmat.de

In-Situ-Grown Cu Dendrites Plasmonically Enhance Electrocatalytic Hydrogen Evolution on Facet-Engineered Cu_2O

Hao Zhang, Jiefeng Diao, Yonghui Liu, Han Zhao, Bryan K. Y. Ng, Zhiyuan Ding, Zhenyu Guo, Huanxin Li, Jun Jia, Chang Yu, Fang Xie, Graeme Henkelman, Maria-Magdalena Titirici, John Robertson, Peter Nellist, Chunying Duan, Yuzheng Guo,* D. Jason Riley,* and Jieshan Qiu**

Herein, facet-engineered Cu_2O nanostructures are synthesized by wet chemical methods for electrocatalytic HER, and it is found that the octahedral Cu_2O nanostructures with exposed crystal planes of (111) (O-Cu_2O) has the best hydrogen evolution performance. Operando Raman spectroscopy and ex-situ characterization techniques showed that Cu_2O is reduced during HER, in which Cu dendrites are grown on the surface of the Cu_2O nanostructures, resulting in the better HER performance of O-Cu_2O after HER (O-Cu_2O-A) compared with that of the as-prepared O-Cu_2O. Under illumination, the onset potential of O-Cu_2O-A is ca. 52 mV positive than that of O-Cu_2O, which is induced by the plasmon-activated electrochemical system consisting of Cu_2O and the in-situ generated Cu dendrites. Incident photon-to-current efficiency (IPCE) measurements and the simulated UV–Vis spectrum demonstrate the hot electron injection (HEI) from Cu dendrites to Cu_2O. Ab initio nonadiabatic molecular dynamics (NAMD) simulations revealed the transfer of photogenerated electrons (27 fs) from Cu dendrites to Cu_2O nanostructures is faster than electron relaxation (170 fs), enhancing its surface plasmons activity, and the HEI of Cu dendrites increases the charge density of Cu_2O. These make the energy level of the catalyst be closer to that of H^+/H_2, evidenced by the plasmon-enhanced HER electrocatalytic activity.

1. Introduction

Cu_2O is a non-toxic 3d transition metal oxide with interesting properties, which is low-price and abundant on Earth compared with noble metals.[1–3] Cu_2O also has sufficient redox capacity, abundant surface active sites, and easily tunable morphology, porosity, and particle size.[4,5] It has been reported that p-type Cu_2O is a potential material for catalytic applications that are environmentally beneficial, including photocatalytic hydrogen production,[6–8] electrocatalytic CO_2 reduction,[9–11] electrocatalytic OER and ORR.[12–16] However, n-type Cu_2O as an electrocatalyst has attracted less attention. To date the hydrogen evolution reaction (HER) performance of n-type Cu_2O-based electrocatalysts is poor, and the active sites and catalytic mechanism of these catalysts are still unclear due to the limitation of characterization techniques.[17,18]

The atomic arrangement and chemical status of the exposed surface have

H. Zhang, F. Xie, D. J. Riley
Department of Materials and London Center for Nanotechnology
Imperial College London
London SW7 2AZ, UK
E-mail: hao.zhang@chem.ox.ac.uk; jason.riley@imperial.ac.uk

H. Zhang
Chemistry Research Laboratory
Department of Chemistry
University of Oxford
Oxford OX1 3TA, UK

The ORCID identification number(s) for the author(s) of this article can be found under https://doi.org/10.1002/adma.202305742

© 2023 The Authors. Advanced Materials published by Wiley-VCH GmbH. This is an open access article under the terms of the Creative Commons Attribution License, which permits use, distribution and reproduction in any medium, provided the original work is properly cited.

DOI: 10.1002/adma.202305742

J. Diao, G. Henkelman
Department of Chemistry and the Oden Institute for Computational Engineering and Sciences
The University of Texas at Austin
Austin, TX 78712, USA

Y. Liu, J. Jia, J. Robertson, Y. Guo
School of Electrical Engineering and Automation
Wuhan University
Wuhan 430072, P. R. China
E-mail: yguo@whu.edu.cn

H. Zhao
Department of Chemistry
University of Zurich
Winterthurerstrasse 190, Zurich CH-8057, Switzerland

B. K. Y. Ng
Wolfson Catalysis Centre
Department of Chemistry
University of Oxford
Oxford OX1 3QR, UK

 © 2023 The Authors. Advanced Materials published by Wiley-VCH GmbH

a great influence on the performance of electrocatalysts,[19–24] including atomic steps, corners, edges, coordination states, dangling bonds, and surface energy. Preferentially exposing some specific faces with high energy can increase the reaction rate.[25–27] For example, Wang and co-workers proposed an in situ electrochemical reduction strategy to synthesize Pt nanosheets with high-index {311} planes and low-index {200} and {111} planes on carbon nanotubes, and it is found that the {311} planes of Pt nanosheets had a higher electrocatalytic hydrogen evolution activity compared with the other planes.[28] Kuo et al. prepared {100} facet-dominated silver nanocubes and {111} facet-dominated silver nano octahedra via polyol reactions. The results showed that plasmonic Ag NOs with exposed {111} facets exhibited better catalytic performance for HER than Ag NCs with exposed {100} facets.[29] However, most catalysts consist of crystals with mixed facets, showing an averaged catalytic activity. To investigate the influence of crystal facets, it is necessary to control the anisotropic structure of catalysts with specific crystal planes.

Recently, it has been found that light can be used as the driving force of electrochemical reactions. For example, Ag nanocubes harvested visible light and directly drove catalytic oxidation reactions of CO and NH_3.[30] Au nanoparticles served as both the light absorber and electrocatalytic active site to promote the occurrence of efficient electrochemical reaction of glucose electrooxidation by utilizing the energy of hot carriers.[31] Au nanorods filled O_2 antibonding orbitals using exciting hot electrons by absorbing visible light, thereby activating O—O bonds and enhancing the oxygen reduction activity of Pt.[32] However, the current electrocatalytic studies of Cu_2O have focused on stand-alone electrocatalysis and ignored integration with light, especially the localized surface plasmon resonance (LSPR), to the electrocatalysis systems.[33–35] LSPR is the collective oscillatory behavior of conduction electrons in metallic nanostructures driven by incident light,[36] and it can provide unique benefits for semiconductor nanostructures, including enhanced local electromagnetic fields, efficient charge carrier separation, and thermal effects during photon dissipation,[37–39] all resulting in accelerated electrochemical processes.[40–42] Therefore, introducing the plasmonic effect into Cu_2O is an effective method to promote the overall electrocatalytic process.

Herein, cubic, truncated octahedral and octahedral Cu_2O particles (C-Cu_2O, T-Cu_2O, O-Cu_2O) with different crystal effects were synthesized by a wet chemical method, in which $NH_2OH{\cdot}HCl$ acts as both reducing agent and morphology control agent. The structures and chemical compositions of the Cu_2O nanostructures were compared through detailed characterization. The hydrogen evolution performance of the three samples was tested in an alkaline environment. The adsorption-free energy of hydrogen intermediates on different crystal facets was calculated and RLS was determined by density functional theory (DFT). Post-mortem investigations including ex situ characterization and operando Raman spectroscopy studied the changes in structure, composition, and bandgap of the samples during HER, and identified the active site of the reaction. DFT calculations investigated the charge transfer at the Cu_2O/Cu interface. The hydrogen evolution performance of O-Cu_2O before and after HER was compared under light and dark conditions, respectively, and it was proved that the superior HER performance of O-Cu_2O-A was due to the plasmon enhancement effect of Cu dendrites and the formation of Cu_2O/Cu heterostructures.

2. Results and Discussion

2.1. Structural Characterization and Chemical Analysis

Cu_2O nanostructures with different exposed crystal facets were synthesized by the wet chemical method, and the synthetic route is shown in **Figure 1**. $CuCl_2$, SDS, NaOH, and $NH_2OH{\cdot}HCl$ were sequentially added to deionized water, and Cu_2O particles were obtained by chemical reduction. By gradually increasing the content of reducing agent $NH_2OH{\cdot}HCl$, three Cu_2O samples with different morphologies were prepared, which were cubic, truncated octahedral, and octahedral Cu_2O (C-Cu_2O, T-Cu_2O, O-Cu_2O). Field-emission scanning electron microscopy (FESEM) images show that the Cu_2O nanostructures were uniform and with narrow size distribution, with average sizes of 300, 370, and 400 nm, respectively (**Figure 2**a–c). Transmission electron microscopy (TEM) images (Figure 2a–c, inset) show that the Cu_2O nanostructures are all solid. High-angle annular dark-field scanning transmission electron microscopy (HAADF-STEM) images and the corresponding atomic models highlighting the (111) and (100) facets of Cu_2O are shown in Figure 2d,e, respectively, where each contrast site is contributed by only one atom. Each O atom is surrounded by six Cu atoms in the plan view of (111) facets, while each O atom is surrounded by four Cu atoms in the plan view of (100) facets. With increasing $NH_2OH{\cdot}HCl$ concentration, the exposed (100) crystal plane disappeared and the (111) crystal plane appeared. This trend is attributed to two parts: i) The binding energy of SO_4^{2-} (the functional group of SDS) and Cu^{2+} to (111) facets are 0.434 and 0.503 eV (Figure 2f,g), respectively; the binding energy of SO_4^{2-} and Cu^{2+} to (100) facets are −0.392 and −0.994 eV, respectively (Figure 2h,i). The binding energy of SO_4^{2-} to the (111) crystal plane is lower than that of Cu^{2+}, indicating that SDS is more conducive to occupying the binding site of the (111) crystal plane,[43,44] thus adsorbing on the (111)

Z. Ding, P. Nellist
Department of Materials
University of Oxford
Oxford OX1 3PH, UK
Z. Guo, M.-M. Titirici
Department of Chemical Engineering
Imperial College London
London SW7 2AZ, UK
H. Li, J. Robertson
Department of Engineering
University of Cambridge
Cambridge CB2 1PZ, UK
C. Yu, J. Qiu
State Key Lab of Fine Chemicals
School of Chemical Engineering
Liaoning Key Lab for Energy Materials and Chemical Engineering
Dalian University of Technology
Dalian 116024, P. R. China
E-mail: jqiu@dlut.edu.cn
C. Duan
School of Chemistry
Dalian University of Technology
Dalian, Liaoning 116024, P. R. China

© 2023 The Authors. Advanced Materials published by Wiley-VCH GmbH

15214095, 2023, 42, Downloaded from https://onlinelibrary.wiley.com/doi/10.1002/adma.202305742 by Test, Wiley Online Library on [27/10/2023]. See the Terms and Conditions (https://onlinelibrary.wiley.com/terms-and-conditions) on Wiley Online Library for rules of use; OA articles are governed by the applicable Creative Commons License

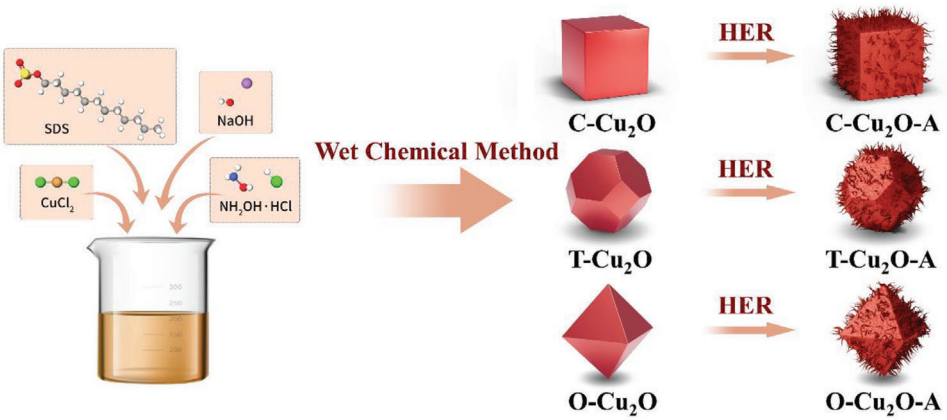

Figure 1. Schematic diagram of the synthesis of C-Cu_2O, T-Cu_2O, O-Cu_2O and C-Cu_2O-A, T-Cu_2O-A, O-Cu_2O-A.

plane to stabilize the surface; on the contrary, the binding energy of Cu^{2+} to the (100) crystal plane is lower compared with that of SO_4^{2-}, which indicates that Cu^{2+} is more favorable to adsorb on the (100) crystal plane and is reduced by $NH_2OH{\cdot}HCl$, resulting to the growth of the (100) crystal plane. ii) The surface energies of Cu_2O (111) and Cu_2O (100) facets are 0.023 and 0.057 eV, respectively. The lower surface energy of the Cu_2O (111) plane indicates that it is more stable, which is also responsible for the increase in the proportion of (111) planes during crystal growth.[45] The powder X-ray diffraction (XRD) pattern of Cu_2O nanostructures is shown in **Figure 3**a. Five distinct peaks at $2\theta = 29.5°$, 36.4°, 42.3°, 61.3°, and 73.5° correspond to (110), (111), (200), (220),

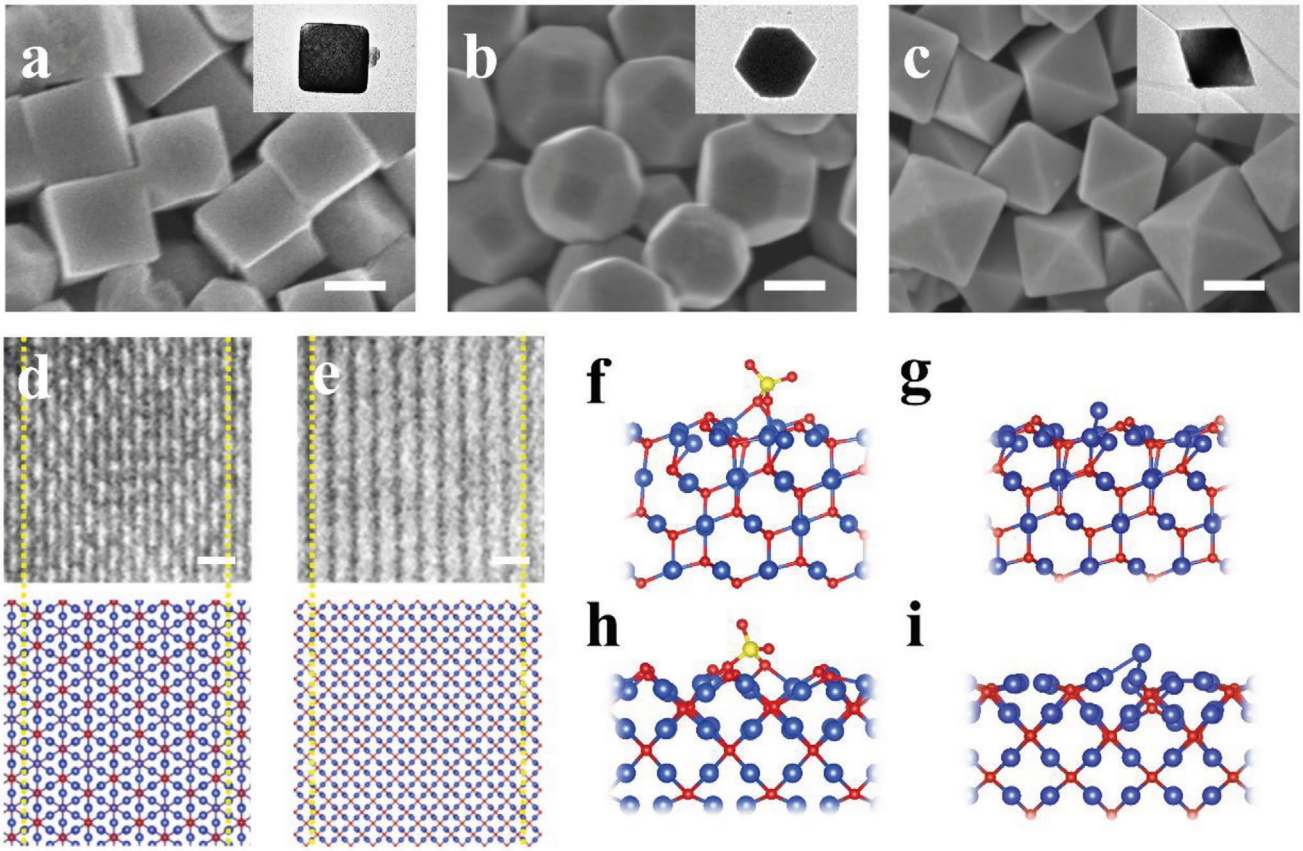

Figure 2. Crystal structure characterization. a–c) FESEM and TEM images (inset) of C-Cu_2O (a), T-Cu_2O (b), and O-Cu_2O (c) (scale bars: 200 nm). d,e) HAADF-STEM images and the corresponding atomic models of (111) facets (d) and (100) facets (e) of Cu_2O (scale bars: 0.5 nm). f–i) Adsorption structures of SO_4^{2-} (f) and Cu^{2+} (g) on Cu_2O (111) facets, and h,i) SO_4^{2-} (h) and Cu^{2+} (i) on Cu_2O (100) facets.

 © 2023 The Authors. Advanced Materials published by Wiley-VCH GmbH

15214095, 2023, 42, Downloaded from https://onlinelibrary.wiley.com/doi/10.1002/adma.202305742 by Test, Wiley Online Library on [27/10/2023]. See the Terms and Conditions (https://onlinelibrary.wiley.com/terms-and-conditions) on Wiley Online Library for rules of use; OA articles are governed by the applicable Creative Commons License

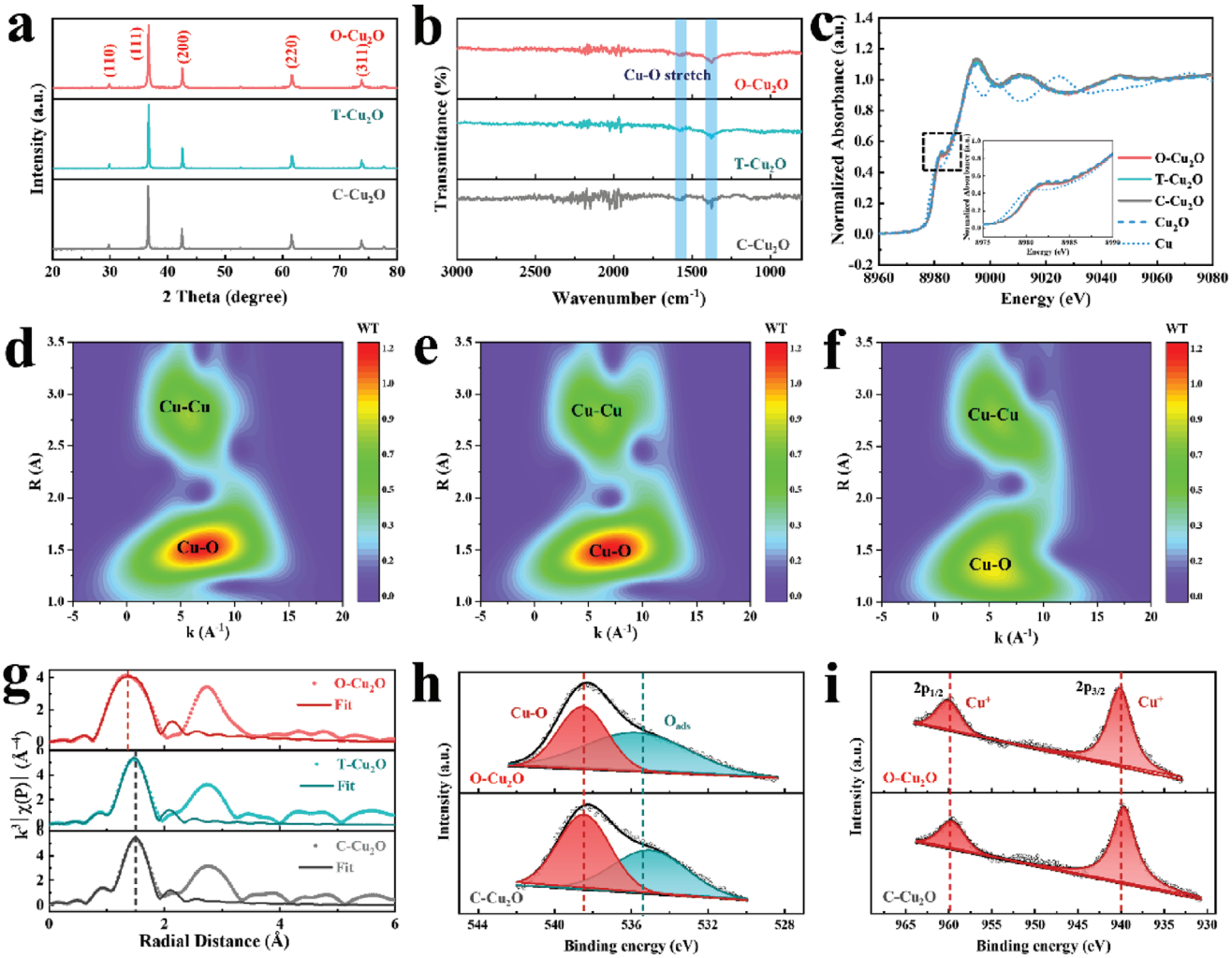

Figure 3. Chemical composition analysis. a) XRD patterns and b) FT-IR spectra of C-Cu_2O, T-Cu_2O and O-Cu_2O. c) Cu *K*-edge XANES spectra of C-Cu_2O, T-Cu_2O, O-Cu_2O, Cu_2O, and Cu foil (inset: an enlarged view of the dashed box). d–f) Wavelet transform-EXAFS spectra of *K*-edge of C-Cu_2O (d), T-Cu_2O (e), and O-Cu_2O (f). g) *R*-space FT-EXAFS spectra of Cu *K*-edge of C-Cu_2O, T-Cu_2O and O-Cu_2O. h,i) XPS high-resolution spectra at O 1s edge (h) and Cu 2p edge (i) of C-Cu_2O and O-Cu_2O.

and (311) planes of Cu_2O (JCPDS card No. 05–0667), respectively. The diffraction peaks of Cu_2O are sharp and intense, indicating it is highly crystalline. The peaks at 1573 and 1376 cm^{-1} in the Fourier-transform infrared (FT-IR) spectroscopy of Cu_2O nanostructures (Figure 3b) were assigned to the Cu—O stretching mode,[46,47] and no impurity peaks were observed, confirming the high purity of the product. Scanning transmission electron microscopy attached with energy dispersive spectroscopy (STEM-EDS) results demonstrate that the Cu_2O samples were composed of the elements Cu and O without impurities (Figure S1, Supporting Information).

X-ray absorption spectroscopy (XAS) was performed to further study the different exposed facets. First, by comparing the near-edge regions of C-Cu_2O, T-Cu_2O, and O-Cu_2O with Cu foil and Cu_2O (Figure 3c), it confirms that Cu_2O of high purity was synthesized. Wavelet analysis of the XAS data (Figure 3d–f) indicates the similarity between the three facets, with peaks near (6 $Å^{-1}$, 1.5 Å) attributed to first shell Cu–O scattering, and peaks near (6 $Å^{-1}$, 2.8 Å) attributed to second shell scattering. Their similarity in peak intensities and positions indicates their resemblance in structures. However, for O-Cu_2O, a reduction in intensity along with a broader peak width is observed. Fitting on the *R*-space of the X-ray absorption fine structure (XAFS) data is then performed to quantify the changes in scattering paths (Figure 3g), with the fitting parameters and *k*-space fitting available in Figure S2 and Tables S1–S3 (Supporting Information). For C-Cu_2O, a coordination number of 1.93(63) at 1.83(5) Å from Cu is observed, which falls slightly shorter than the expected value of 2 for Cu_2O. As the fraction of exposed (111) facets increases to T-Cu_2O and O-Cu_2O, an increase of coordination number of 2.07(68) and 2.23(63) at 1.86(4) and 1.87(4) Å from Cu was obtained. An exposed (100) facet would result in undercoordinated Cu near the boundaries of the nanostructures, whereas the exposed (111) facet would see fully coordinated Cu, aligning well with our fitted experimental observations. Figure 3h shows the O 2p X-ray photoelectron spectroscopy (XPS) signals of the C-Cu_2O and

 © 2023 The Authors. Advanced Materials published by Wiley-VCH GmbH

15214095, 2023, 42, Downloaded from https://onlinelibrary.wiley.com/doi/10.1002/adma.202305742 by Test, Wiley Online Library on [27/10/2023]. See the Terms and Conditions (https://onlinelibrary.wiley.com/terms-and-conditions) on Wiley Online Library for rules of use; OA articles are governed by the applicable Creative Commons License

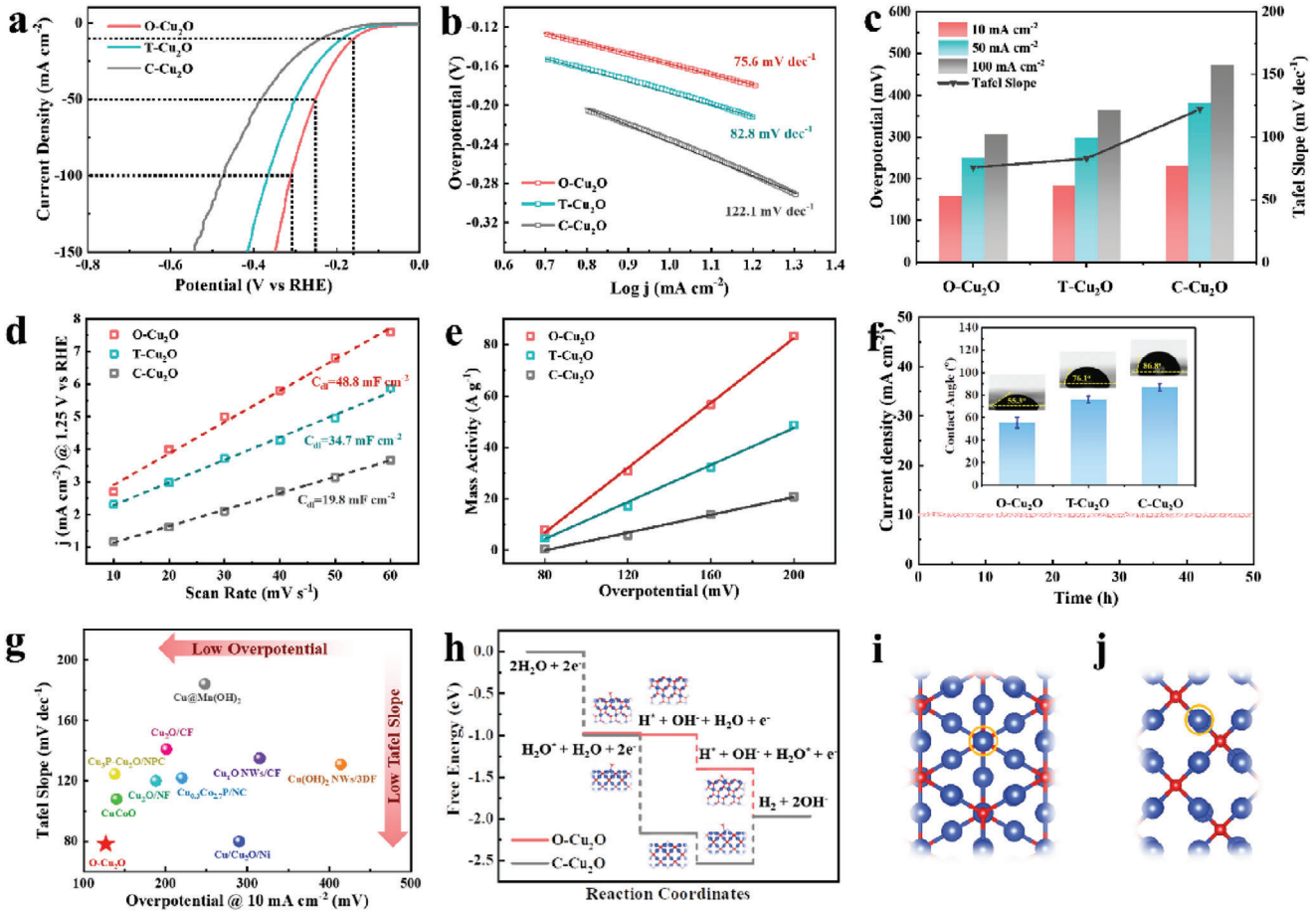

Figure 4. Electrochemical performance for HER. a) Polarization curves and b) Tafel plots of C-Cu_2O, T-Cu_2O, and O-Cu_2O in alkaline electrolyte. The FTO glass coated with the Cu_2O samples, a graphite rod, and an Hg/HgO/OH^- electrode were employed as the working electrode, counter electrode, and reference electrode, respectively in all the measurements. c) Comparison of Tafel slopes and the overpotentials needed to deliver cathodic current densities of 10, 50, and 100 mA cm^{-2} for C-Cu_2O, T-Cu_2O, and O-Cu_2O. d) Capacitive current measured at 0.25 V vs RHE for C-Cu_2O, T-Cu_2O and O-Cu_2O as a function of scan rate. e) Mass activity of C-Cu_2O, T-Cu_2O and O-Cu_2O. f) Chronoamperometry measurement of O-Cu_2O at an applied voltage of −0.16 V vs RHE (inset: electrolyte contact angle measurements of C-Cu_2O, T-Cu_2O, and O-Cu_2O). g) Comparison of HER activity with some recently reported Cu-based catalysts in alkaline electrolyte. h) Gibbs free energy diagrams of C-Cu_2O, T-Cu_2O and O-Cu_2O for HER in alkaline electrolyte. i,j) Bader charge analysis of (111) facets (i) and (100) facets (j) of Cu_2O, and the Cu active sites are highlighted by the orange circles.

O-Cu_2O nanostructures with different exposed facets, which can be divided into two peaks, corresponding to the Cu—O bond and the adsorbed oxygen, respectively.[48] For the Cu 2p signals (Figure 3i) of C-Cu_2O and O-Cu_2O, they are divided into two peaks, attributing to Cu^+ of Cu $2p_{1/2}$ and Cu $2p_{3/2}$, respectively.[49,50]

2.2. Evaluation of the Electrochemical HER Performance

The electrocatalytic HER performance of the three Cu_2O catalysts was investigated by using a standard three-electrode system in 1.0 M KOH. The FTO glass coated with the Cu_2O samples was served as the working electrode, and a graphite rod and an Hg/HgO/OH^- electrode were employed as the counter electrode and reference electrode, respectively. The linear sweep voltammetry (LSV) curves of the three Cu_2O samples are shown in **Figure 4**a. It is found that O-Cu_2O with (111) exposed facets exhibits the best activity, and the overpotentials of O-Cu_2O were 158, 250, and 307 mV for current densities of 10, 50, and 100 mA cm^{-2}, respectively, while the overpotentials for the same current densities for C-Cu_2O and T-Cu_2O were 231, 184; 382, 299; and 472, 364 mV, respectively. O-Cu_2O also exhibited a relatively small Tafel slope (75.6 mV dec^{-1}) compared with C-Cu_2O (122.1 mV dec^{-1}) and T-Cu_2O (82.8 mV dec^{-1}), which further supports its faster HER reaction rate (Figure 4b,c, Table S4, Supporting Information). For the convenience of comparison with the literature, Cu_2O samples were prepared as slurries and drop-coated on the glassy carbon electrode (GCE) for testing and the results are shown in Figure S3 (Supporting Information). By comparing the hydrogen evolution activities of Cu_2O samples on FTO and CCE, it is found that the overpotential of the catalyst on GCE is lower than that on FTO, which may be attributed to the better conductivity of GCE compared to FTO. The HER performance of bare FTO, Nafion-modified FTO, and bare GCE were performed to reveal the influence of substrates, and the polarization curves

 © 2023 The Authors. Advanced Materials published by Wiley-VCH GmbH

15214095, 2023, 42, Downloaded from https://onlinelibrary.wiley.com/doi/10.1002/adma.202305742 by Test, Wiley Online Library on [27/10/2023]. See the Terms and Conditions (https://onlinelibrary.wiley.com/terms-and-conditions) on Wiley Online Library for rules of use; OA articles are governed by the applicable Creative Commons License

are shown in Figure S4 (Supporting Information). It is found that their overpotentials of bare FTO, Nafion-modified FTO, and bare GCE were 380, 382, and 347 mV, respectively, indicating that the addition of Nafion had little effect on HER activity, and bare GCE has better HER activity than bare FTO, which may be due to the better conductivity of GCE electrode. This is consistent with the HER activity of the electrodes loaded with Cu_2O samples.

The intrinsic catalytic activity of the Cu_2O samples was evaluated by the electrochemically active surface area (ECSA) and mass activity. ECSA is proportional to the double-layer capacitance (C_{dl}), which is calculated from cyclic voltammetry curves (Figure 4d; Figure S5, Supporting Information).[51] The C_{dl} of O-Cu_2O is 48.8 mF cm^{-2}, which is higher than that of C-Cu_2O (19.8 mF cm^{-2}) and T-Cu_2O (34.7 mF cm^{-2}). The mass activity of O-Cu_2O at an overpotential of 120 mV is 30.7 A g^{-1}, which is better than that of C-Cu_2O (5.8 A g^{-1}) and T-Cu_2O (17.1 A g^{-1}) (Figure 4e). The TOF of C-Cu_2O, T-Cu_2O, and O-Cu_2O are 0.232, 0.505 and 0.851 s^{-1} per site at an overpotential of 200 mV, respectively, and the TOF of O-Cu_2O is ≈4 times that of C-Cu_2O. It is worth mentioning that the determined intrinsic activity values are inevitably underestimated as active sites are endowed only by surface metal species, rather than the entire transition metal component.[52] LSV curves of the Cu_2O samples in Figure 4a have been normalized to the ECSA (Figure S6, Supporting Information), O-Cu_2O still exhibited the highest current density under the same voltage condition, indicating its best activity among the Cu_2O samples. The exchange current density was obtained from the Tafel plots after ECSA normalization (Figure S7, Supporting Information), and the values of C-Cu_2O, T-Cu_2O, and O-Cu_2O are 0.574, 0.440 and 0.296 mA cm^{-2}, respectively. The higher value of O-Cu_2O reveals its higher HER kinetics. Electrolyte contact angle tests show that O-Cu_2O is more hydrophilic than C-Cu_2O and T-Cu_2O (Figure 4f, inset), which may be because the (111) crystal plane has a higher atomic arrangement density than the (100) crystal plane, resulting in its relatively lower surface energy.[53] Chronoamperometry measurements were used to investigate the stability of O-Cu_2O under an applied voltage of −0.16 V vs reversible hydrogen electrode (RHE) (Figure 4f), and there was no obvious degradation after the 50 h test, indicating good durability. The HER activity of the obtained O-Cu_2O compares favorably to most previously reported Cu-based HER electrocatalysts (Figure 4g, Table S5, Supporting Information).

As shown in Figure 4h, the free energy differences of the first H_2O molecular adsorption, the Volmer step, the second H_2O molecular adsorption and the Heyrovsky step in the HER process on the Cu_2O (111) facets are −0.965, −0.027, −0.412 and −0.566 eV, respectively. However, the free energy differences of the same four steps on the Cu_2O (100) planes are −0.996, −1.177, −0.365, and 0.567 eV, respectively. The last step on the Cu_2O (100) planes has a positive free energy difference, indicating that the Heyrovsky step (RLS) on Cu_2O (100) facets has a much higher energy barrier than that on Cu_2O (111) facets, leading to its relatively poor HER activity. The partial charges of active Cu sites on Cu_2O (111) and Cu_2O (100) facets were calculated using Bader charge analysis (Figure 4i,j). The partial charges of the Cu active sites on the (111) and (100) facets of Cu_2O are +0.398 and +0.235 e, respectively. The less positive partial charge of the Cu site on Cu_2O (100) indicates more electrons on it, thus forming a stronger covalent bond with H, resulting in a stable H^* intermediate. However, the overly stable H^* intermediate makes the desorption of H difficult, which gives rise to a high energy barrier for the Heyrovsky step on Cu_2O (100).

2.3. Active Site Identification

To elucidate the catalytic active sites, the microstructure, chemical composition, and valence evolution of the O-Cu_2O catalyst after HER testing (O-Cu_2O-A) in alkaline electrolyte were investigated by post-mortem characterization. SEM images (**Figure 5**a) demonstrate that dendrites were grown on the surface of the three Cu_2O samples after long-term chronoamperometry HER tests, and no obvious fragmentation was observed. TEM images (Figure 5b,c; Figure S5a,c, Supporting Information) indicate the length of the dendrites is ≈5–10 nm, while the solid shape of the Cu_2O samples after HER remains unchanged. The high-resolution TEM (HRTEM) image (Figure 5c, inset) reveals the heterostructure at the interface of the solid structure and the dendrites. The lattice spacings of 0.24 and 0.21 Å correspond to the (111) planes of Cu_2O and Cu, respectively, indicating the generated dendrites are Cu, formed by the reduction of Cu_2O. Selected-area electron diffraction (SAED) pattern (Figure 5d) shows the single-crystal structure of O-Cu_2O-A, and the STEM image and elemental mapping (Figure 5e; Figure S8b,d, Supporting Information) show that the chemical composition of the Cu_2O samples remains unchanged after HER, still consisting of O and Cu. HAADF-STEM image of O-Cu_2O-A and the corresponding atomic model are shown in Figure 5f, and oxygen vacancies appear after the HER test, which is marked with yellow hexagons. XRD was conducted to analyze the crystal structure of O-Cu_2O after HER. As shown in **Figure 6**a, compared with the XRD pattern of O-Cu_2O, the additional peaks of O-Cu_2O-A at 43.3°, 50.4° and 74.0° correspond to the (111), (200) and (220) crystal planes of Cu (JCPDS card No. 04-0836), indicating that Cu_2O reduction occurred during the test, which is consistent with the HRTEM results and further proves that the observed dendrites are Cu crystals. From the FT-IR spectra of O-Cu_2O before and after HER (Figure 6b), it was found that the sample after the HER test showed a Cu—Cu stretching mode at 1137 cm^{-1},[54,55] suggesting the formation of Cu. As shown in Figure 6c, the specific surface areas of O-Cu_2O and O-Cu_2O-A were 58.05 and 110.24 m^2 g^{-1}, respectively, and the pore volumes of the samples before and after cycling were 0.032 and 0.107 cm^3 g^{-1}, respectively, suggesting a significant increase in the pore structure of the sample after HER. The pore diameters were mainly distributed ≈0.2 nm, indicating the existence of a large number of micropores (Figure S9, Supporting Information).[56]

Operando Raman spectroscopy was performed to explore the chemical composition evolution of O-Cu_2O in real-time HER (Figure 6d). The peaks at 111 and 218 cm^{-1} are attributed to the A_{1g} vibration modes of the Cu—O and Cu—Cu bonds, respectively.[57] When the voltage changed from 0 to −0.2 V vs RHE, the peak intensity of the Cu—O bond essentially remained unchanged, while that of the Cu—Cu bond increased significantly, and the E_g vibration mode of the Cu—Cu bond appeared,[58,59] further proving the formation of Cu. The fitted XPS spectra of O 1s orbital for O-Cu_2O and O-Cu_2O-A are compared in Figure 6e, an additional oxygen vacancy (O_v) peak

© 2023 The Authors. Advanced Materials published by Wiley-VCH GmbH

15214095, 2023, 42, Downloaded from https://onlinelibrary.wiley.com/doi/10.1002/adma.202305742 by Test, Wiley Online Library on [27/10/2023]. See the Terms and Conditions (https://onlinelibrary.wiley.com/terms-and-conditions) on Wiley Online Library for rules of use; OA articles are governed by the applicable Creative Commons License

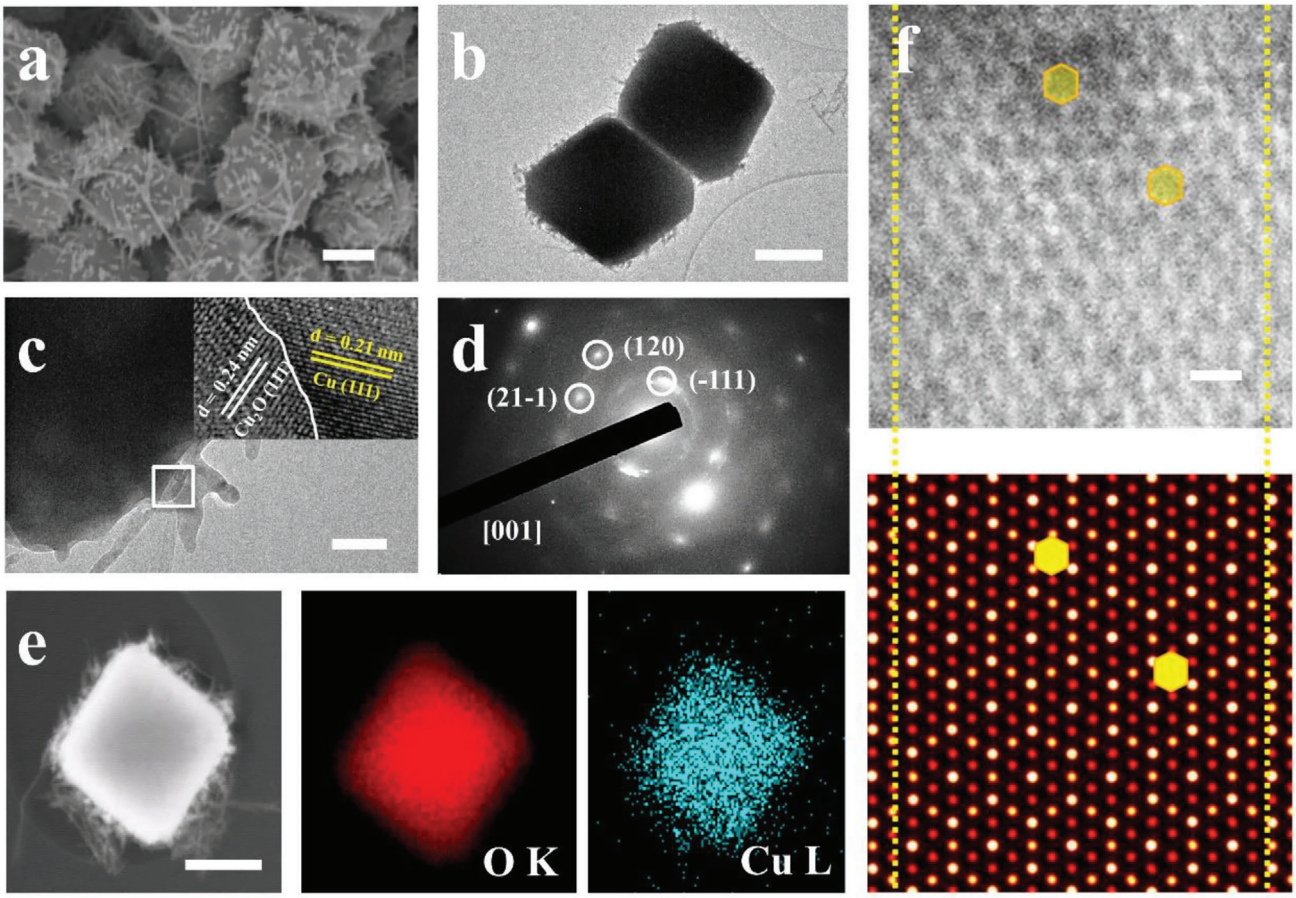

Figure 5. Crystal structure characterization after HER. a) FESEM and b) TEM images of O-Cu_2O-A (scale bars: 200 nm). c) HRTEM image and d) SAED pattern of O-Cu_2O-A (scale bar: 5 nm). e) STEM and elemental mapping images of O-Cu_2O-A (scale bar: 200 nm). f) HAADF-STEM image of O-Cu_2O-A and the corresponding simulated atomic model (scale bar: 0.5 nm), and the yellow hexagons represent oxygen vacancies.

appears in O-Cu_2O-A, which may be due to the lack of lattice oxygen during the reduction of Cu_2O, and this is consistent with the HAADF-STEM result.[60] The peak of Cu^0 appears in the Cu 2p orbital spectrum of O-Cu_2O-A (Figure 6f),[61] indicating the formation of Cu. This is consistent with the results of HRTEM, XRD, and FT-IR, which proves that Cu_2O is reduced to Cu during the HER process. The peak of the UV–vis spectrum of O-Cu_2O-A redshifted compared with that of O-Cu_2O, and the bandgap decreased from 2.57 eV (O-Cu_2O) to 2.50 eV (O-Cu_2O-A), indicating that the formation of Cu dendrites enhanced the conductivity of the catalyst (Figure S10, Supporting Information).

XAS analysis was performed on O-Cu_2O-A for the characterization of O-Cu_2O after HER. The near-edge region of O-Cu_2O-A is significantly different from that of Cu_2O (Figure 6g), suggesting the structure has deviated from Cu_2O upon catalyst cycling. Comparing the wavelet transform of O-Cu_2O and O-Cu_2O-A (Figures 3f and 6h), a shift of the peak from (5.5 $Å^{-1}$, 2.78 Å) to (5.5 $Å^{-1}$, 2.53 Å) was detected, along with an enhanced intensity of the peak centered from (5.2 $Å^{-1}$, 1.34 Å) to (6.05 $Å^{-1}$, 1.47 Å), which can be explained by the shortened Cu—Cu distance from Cu_2O (3.03 Å) compared to Cu metal (2.56 Å). Further quantification with XAFS fitting of O-Cu_2O-A (Figure 6i, Table S6, Supporting Information) shows a much higher Cu—O first shell coordination number (3.13) compared to O-Cu_2O (2.23) (Figure 3g, Figure S2, Supporting Information), which may be attributed to the formation of $Cu(OH)_2$ phases during catalysis cycling. Intriguingly, a good fitting (*R*-factor 2.38%) can be obtained with two Cu—Cu scattering paths from Cu foil and Cu_2O between 2–3.5 Å for O-Cu_2O-A (Figures S11, S12, Supporting Information). Cu—Cu scattering from Cu foil is seen at 2.67(4) Å with a coordination number of 3.0(4), while another Cu—Cu scattering from Cu_2O is seen at 3.19(13) Å with a coordination number of 9.9(45). The observed Cu—Cu scattering from both Cu foil and Cu_2O echoes with the observed Cu dendrites on the surface of Cu_2O aforementioned characterized by other experimental techniques.

Figure 6j shows the density of states of plain Cu_2O and Cu_2O (111) with one layer of Cu (111) deposition, as a model of Cu_2O (111) before and after HER tests. The main difference between the two models lies in the Fermi surface. With Cu (111) deposition after cycles, more unoccupied states appear near the Fermi surface, leading to higher electron conductivity. This is beneficial for the electron-involved steps (Volmer and Heyrovsky) and contributes to the higher activity of Cu_2O (111) after HER tests. The charge-transfer diagram shows a remarkable charge transfer between the Cu (111) layer and the Cu_2O (111) facet, in which

 © 2023 The Authors. Advanced Materials published by Wiley-VCH GmbH

15214095, 2023, 42, Downloaded from https://onlinelibrary.wiley.com/doi/10.1002/adma.202305742 by Test, Wiley Online Library on [27/10/2023]. See the Terms and Conditions (https://onlinelibrary.wiley.com/terms-and-conditions) on Wiley Online Library for rules of use; OA articles are governed by the applicable Creative Commons License

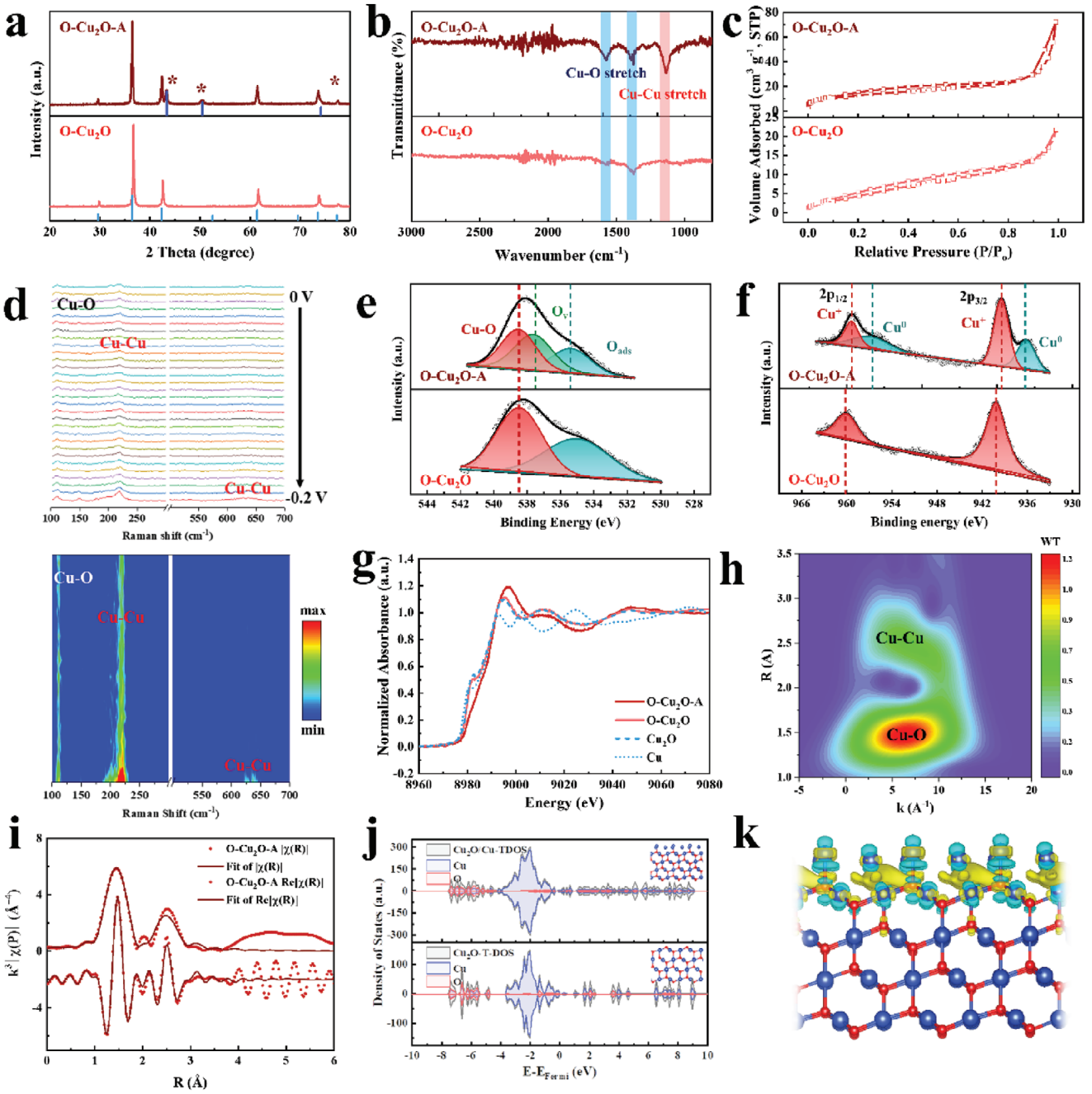

Figure 6. Chemical composition analysis after HER. a) XRD patterns, b) FT-IR spectra, and c) N_2 adsorption/desorption isotherms of O-Cu_2O and O-Cu_2O-A. d) Operando Raman curves and the corresponding contour plot obtained from the voltage changing from 0 to −0.2 V vs RHE. e,f) XPS high-resolution spectra at O 1s edge (e) and Cu 2p edge (f) of O-Cu_2O and O-Cu_2O-A. g) Cu *K*-edge XANES spectra of O-Cu_2O, O-Cu_2O-A, Cu_2O and Cu foil. h) Wavelet transform-EXAFS spectra of O-Cu_2O-A. i) *R*-space FT-EXAFS spectra of Cu *K*-edge of O-Cu_2O-A. j) DOS of Cu_2O and Cu_2O/Cu (inset: the corresponding optimized structural models). k) Charge-transfer diagram (yellow and blue isosurfaces indicate the gain and loss of electrons) of O-Cu_2O-A at the junction of Cu_2O and Cu.

yellow and blue isosurfaces each indicate the gain and loss of electrons. The partial charge of Cu atoms on the Cu_2O (111) facets before and after Cu (111) deposition was calculated with Bader charge analysis (Figure 6k). The surface Cu atoms of Cu_2O (111) facets with Cu layer have an average partial charge of +0.463 e, compared to that of +0.511 e for the surface Cu atoms of Cu_2O (111) facets without Cu deposition. This result demonstrates that after Cu depositing on Cu_2O (111) facets, the Cu_2O (111) facets gain electrons from the deposited Cu, largely increasing the electron density and resulting in a better electron conductivity on the Cu_2O (111) facets. Moreover, with a proper partial charge on the Cu active sites of Cu_2O (111) facets, the Heyrovsky step (RLS)

 © 2023 The Authors. Advanced Materials published by Wiley-VCH GmbH

15214095, 2023, 42, Downloaded from https://onlinelibrary.wiley.com/doi/10.1002/adma.202305742 by Test, Wiley Online Library on [27/10/2023]. See the Terms and Conditions (https://onlinelibrary.wiley.com/terms-and-conditions) on Wiley Online Library for rules of use; OA articles are governed by the applicable Creative Commons License

energy barrier is reduced by tuning the H- and H_2O^- binding strength, thus contributing to a better HER activity.

2.4. Photoelectrochemical Performance for HER

To explore the effect of the formed Cu dendrites and the Cu_2O/Cu interface on the electrocatalytic hydrogen evolution, the HER performance of O-Cu_2O and O-Cu_2O-A under the conditions with (O-Cu_2O-on, O-Cu_2O-A-on) and without (O-Cu_2O-off, O-Cu_2O-A-off) light was compared. The FTO glass coated with the Cu_2O samples served as the working electrode, and a graphite rod and an Hg/HgO/OH^- electrode were employed as the counter electrode and reference electrode, respectively, and the active surface area 0.28 cm^{-2}. The light source was a 150 W Xe lamp equipped with an AM 1.5 G filter, and the light intensity at the surface of the electrode was 100 mW cm^{-2}. The Cu_2O-based FTO samples were illuminated from the front side (Cu_2O samples) to the back side (FTO substrate). The overpotentials of O-Cu_2O-off and O-Cu_2O-A-off at 10, 50, 100 mA cm^{-2} were 166, 156; 253, 242; 308, 296 mV, respectively (**Figure 7**a,c, Table S7, Supporting Information). The Tafel slopes of O-Cu_2O-off and O-Cu_2O-A-off were 77.3 and 72.1 mV dec^{-1}, respectively (Figure 7b,c, Table S7, Supporting Information), indicating that the formation of Cu dendrites promoted the electrocatalytic performance of O-Cu_2O-A, which is because of the charge transfer from Cu dendrites to Cu_2O revealed by DFT calculations. Under light irradiation, the overpotentials of O-Cu_2O-on and O-Cu_2O-A-on at 10, 50, 100 mA cm^{-2} were 162, 142; 250, 225; 277, 303 mV, respectively (Figure 7a,c, Table S7, Supporting Information). The Tafel slopes of O-Cu_2O-on and O-Cu_2O-A-on were 66.2 and 75.2 mV dec^{-1}, respectively (Figure 7b,c, Table S7, Supporting Information). O-Cu_2O-A-on has better catalytic performance than O-Cu_2O-on. It is worth noting that the onset potential of O-Cu_2O-A-on is ≈−0.073 V, which has a positive shift of ≈52 mV compared to O-Cu_2O-on (−0.125 V), this is due to the charge-transfer effect at the Cu_2O/Cu interface and the plasmonic enhancement of the formed Cu dendrites. From Figure S13 (Supporting Information), the electrocatalytic HER performance of O-Cu_2O under natural light, dark, and illumination conditions is basically the same, indicating that light has no effect on its catalytic performance. Interestingly, the catalytic performance of O-Cu_2O-A under illumination (O-Cu_2O-A-on) is better than that of O-Cu_2O-A in the dark (O-Cu_2O-A-off). The quantified hydrogen evolution yields of O-Cu_2O and O-Cu_2O-A in electrochemical and photoelectrochemical HER are shown in Figure S14 (Supporting Information). It can be found that O-Cu_2O produced basically the same hydrogen with or without light in the same period of time, and the hydrogen yields of O-Cu_2O-A are higher than those of O-Cu_2O no matter whether there is light or not. In addition, with light irradiation, the amount of hydrogen evolution of O-Cu_2O-A is slightly higher than that of the case without light irradiation.

To further explore the plasmonic enhancement effect of Cu dendrites, IPCE was conducted to explore the absorption of light with specific wavelengths by catalytic materials (Figure 7d). The bump in the region of 500–700 nm is overlapped with the range of plasmonic response of Cu nanostructures (Figure S15, Supporting Information), and this range is higher than the bandgap of O-Cu_2O-A (2.50 eV, 496 nm) (Figure S9, Supporting Information), directly demonstrating the hot-electron transfer from Cu dendrites to Cu_2O. The shift of the Cu^+ peaks to lower binding energy in the Cu 2p XPS spectrum of O-Cu_2O-A also indicated hot-electron transfer (Figure 6f). This hot-electron injection (HEI) process produces more efficient electron–hole separation states, which greatly contributes to the HER activity. In addition, the slight enhancement at 300–500 nm may be due to the light scattering caused by the increased light absorption by Cu dendrites.

The physical and chemical mechanisms behind the photogenerated electrons in the wavelength region greater than 500 nm were investigated to elucidate the reasons for the enhanced electrocatalytic HER performance. O-Cu_2O-A was simulated as Cu_{76}-$(Cu_2O)_{24}$, and the photogenerated electron transfer and energy relaxation at the interface of Cu_{76}–$(Cu_2O)_{24}$ is discussed in detail. The projected density of states of Cu_{76}–$(Cu_2O)_{24}$ compounds with separated Cu and Cu_2O are presented in Figure 7e. It is observed that the systems show a metallic property due to the use of a large copper particle. The PDOS peaks corresponding to the blue and pink dotted lines in Figure 7f represent the photoexcited plasmon (donor) state and the electron acceptor state, respectively, whose charge densities are shown in Figure 7f. The photogenerated electron is mainly localized on the copper particle, which exhibits continuous waves. The electron acceptor is completely localized on the Cu_2O system. Figure 7g shows the mechanism for the enhanced HER activity of O-Cu_2O-A under light irradiation, the charge transfer of the Cu_{76}–$(Cu_2O)_{24}$ compound involves five different steps: Process I: Surface plasmons proliferate near-field plasmonic waves at the interface between Cu_{76} and $(Cu_2O)_{24}$, forming electron–hole pairs. The generated high-energy hot electrons are further away from the electronic equilibrium state on Cu_{76} and may have three possible transport channels: Process II: recombination with holes in Cu_{76}; Process III: injection into the conduction band (CB) of $(Cu_2O)_{24}$ semiconductor; Process IV: direct electrochemical reduction of water on Cu_{76}. Process V: The injected hot electrons in the CB of $(Cu_2O)_{24}$ may be relaxed and transferred to the electron-deficient Cu_{76}, returning to its ground state. The contribution of Process IV for the enhancement of photoelectrochemical current is negligible, as Cu is not a good HER catalyst due to the low adsorbed hydrogen coverage on the surface. There is a low Schottky barrier between Cu and Cu_2O, and Cu dendrites are in situ grown on Cu_2O with tight bonding during the electrochemical HER process, and the electron injection from Cu to Cu_2O is faster and more stable due to the strong interaction between Cu and Cu_2O (Process III). The electron relaxation and charge recombination (Process II) are competitive to the electron injection (Process III). The electron relaxation is accompanied by electron–phonon coupling, and this is due to time-dependent fluctuations of the vibrating atomic motions, which is obtained from the Fourier transform (FT) spectra of the plasma state and the electron-acceptor state of Cu_{76}–$(Cu_2O)_{24}$ compounds (Figure 7h).

In order to further investigate the photogeneration carrier dynamics process and determine the timescales of energy relaxation (Process II) and electron transfer (Process III), the time dependence of electron transfer from Cu to Cu_2O was obtained using ab initio nonadiabatic molecular dynamics (NAMD) simulations,[62–66] as shown in Figure 7i,j. The results demonstrate the photoexcited electron transfer from Cu to Cu_2O takes

© 2023 The Authors. Advanced Materials published by Wiley-VCH GmbH

15214095, 2023, 42, Downloaded from https://onlinelibrary.wiley.com/doi/10.1002/adma.202305742 by Test, Wiley Online Library on [27/10/2023]. See the Terms and Conditions (https://onlinelibrary.wiley.com/terms-and-conditions) on Wiley Online Library for rules of use; OA articles are governed by the applicable Creative Commons License

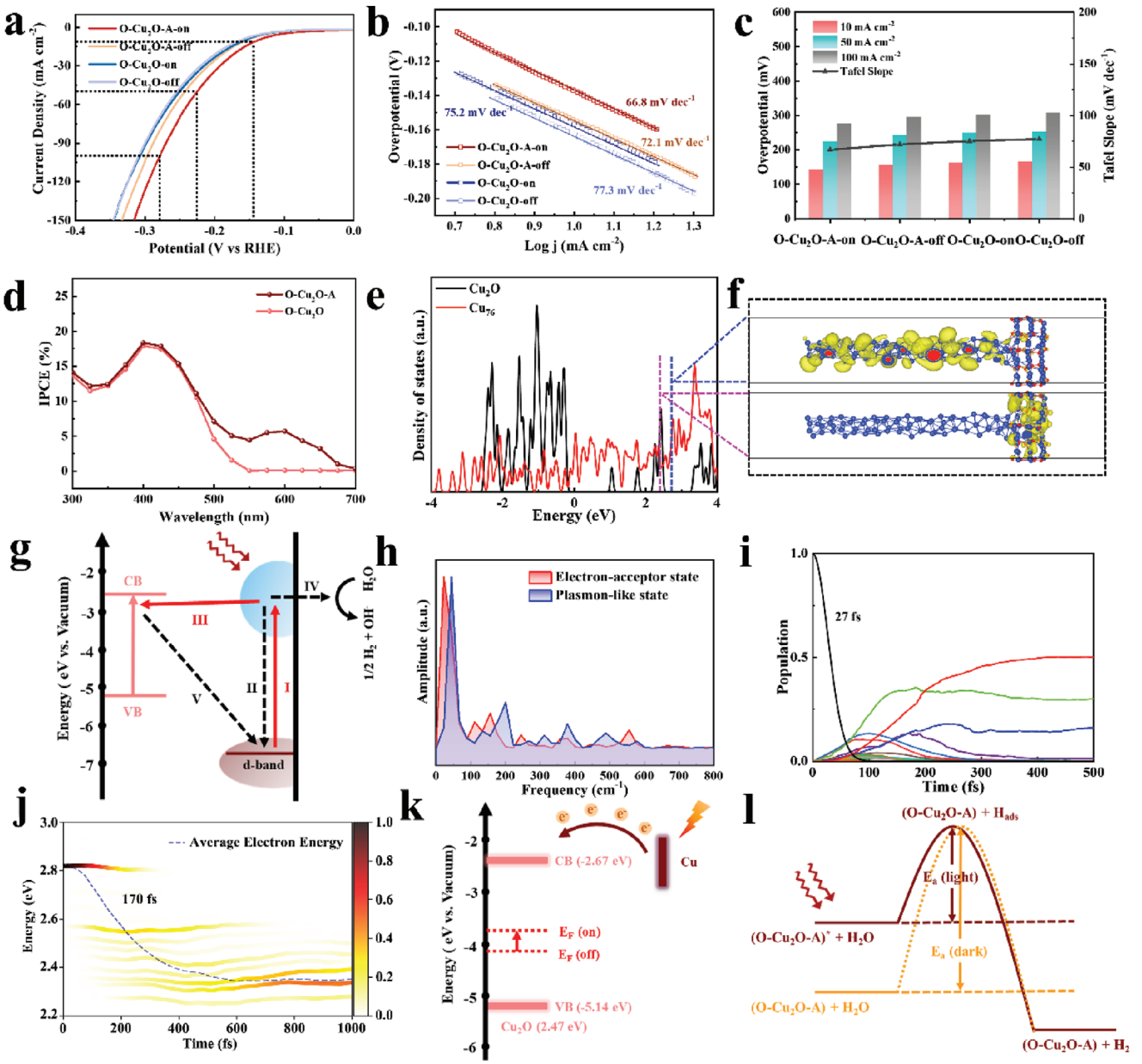

Figure 7. Photoelectrochemical performance for HER. a) Polarization curves and b) Tafel plots of O-Cu_2O and O-Cu_2O-A in the absence or presence of light irradiation in alkaline electrolyte. The FTO glass coated with the Cu_2O samples, a graphite rod, and a Hg/HgO/OH^- electrode were employed as the working electrode, counter electrode, and reference electrode, respectively in all the measurements. c) Comparison of Tafel slopes and the overpotentials needed to deliver cathodic current densities of 10, 50, and 100 mA cm^{-2} for O-Cu_2O and O-Cu_2O-A in the absence or presence of light irradiation. d) IPCE plots measured at 0 V (vs RHE) of O-Cu_2O and O-Cu_2O-A in alkaline electrolyte. e) PDOS of Cu_{76}–$(Cu_2O)_{24}$ and Cu_{76}. f) Photoexcited plasmon-like state and the electron acceptor state corresponding to the peaks of the blue and pink dotted lines in (e). g) Potential hot-electron transfer pathways during SPR. h) Fourier transform spectra of the plasmon-like state (blue) and the electron-acceptor state (red) of Cu_{76}–$(Cu_2O)_{24}$. i) Charge transfer from Cu particle to Cu_2O semiconductors, where black and red lines indicate donor and acceptor states, respectively, and the additional lines represent the states between the donor and the acceptor. j) The energy relaxation between the electron donor and acceptor. The colored strips denote the electron distribution on different energy states, and the dashed line indicates the averaged hole energy. k) Energy level diagram of Cu_2O–Cu illuminating hot-electron injection from Cu to Cu_2O. l) Schematic of the activation energy change of O-Cu_2O-A by light irradiation.

place with 27 fs fitting the population of the initial state. However, the electronic energy relaxation occurs within 170 fs, which is longer than the electron transfer timescales. Due to the low-frequency phonons of heavy Cu atoms, the energy relaxation is slow. Especially, the energy level fluctuations caused by atomic thermal vibration of the system produce electron–phonon coupling at 300 K. Finally, the photogenerated hot-electron transfer from Cu particle to Cu_2O nanomaterials enhances the conductivity of Cu_2O semiconductors, implying that visible light improves its electrocatalytic performance.

 © 2023 The Authors. Advanced Materials published by Wiley-VCH GmbH

15214095, 2023, 42, Downloaded from https://onlinelibrary.wiley.com/doi/10.1002/adma.202305742 by Test, Wiley Online Library on [27/10/2023]. See the Terms and Conditions (https://onlinelibrary.wiley.com/terms-and-conditions) on Wiley Online Library for rules of use; OA articles are governed by the applicable Creative Commons License

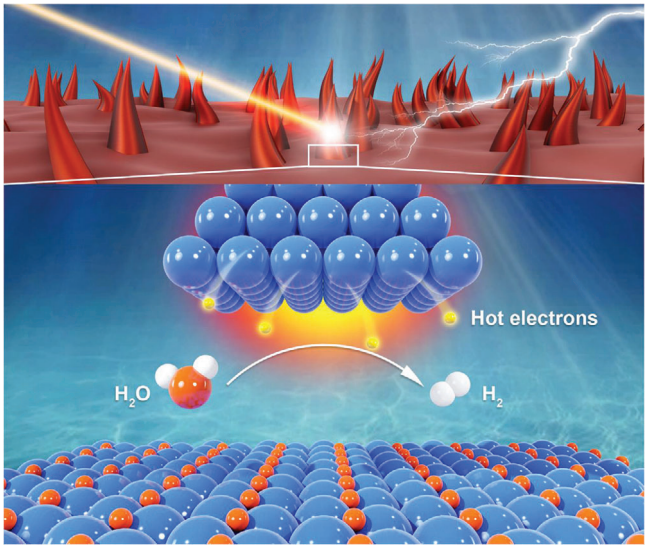

Figure 8. Schematic diagram of hot electron of in-situ-grown Cu dendrites activates the electrocatalytic hydrogen evolution over Cu_2O.

Continuous HEI produces a dynamic charge-separated state, in which the electrons are located at the bottom of the Cu_2O CB and the holes are near the Cu Fermi level. Under illumination, due to the electron injection process of Cu_2O CB, the Fermi level of the semiconductor increases, which is closer to the energy level of the redox pair H^+/H_2, and this reduces the overpotential of O-Cu_2O-A for HER (Figure 7k). In addition, the irradiation power is proportional to the overpotential (Figure S17, Supporting Information), indicating that the direct HEI from Cu dendrites to Cu_2O was accompanied by a decrease in activation energy (Figure 7l), which further demonstrates that the enhancement of HER performance under illumination is mainly due to the electron transfer effect (**Figure 8**).

3. Conclusion

Cu_2O nanostructures with different exposed crystal planes were prepared by wet chemical method and applied to electrocatalytic HER. The effect of exposed crystal planes on their hydrogen evolution performance was explored. It was found that O-Cu_2O with (111) exposed crystal planes had the smallest overpotential and Tafel slope. DFT calculations indicated that this is due to the lower free energy barrier of the Heyrovsky step (RLS) on Cu_2O (111). Post-mortem characterization and Operando Raman spectroscopy were conducted to analyze the changes in crystal structure, chemical composition, and valence state of O-Cu_2O during HER, and thus determined the active sites. It is found that Cu dendrites were reduced on the surface of Cu_2O nanostructures to form a Cu_2O/Cu composite structure. DFT calculations showed that the charge transfer of the Cu_2O/Cu interface promoted its surface electron conductivity and tuned the adsorption strength of HER intermediates, thus greatly enhancing the electrocatalytic HER activity of O-Cu_2O-A. Under light irradiation, ab initio NAMD simulations showed that the charge transfer from Cu dendrites to Cu_2O nanostructures is faster than charge relaxation, improving its surface plasmon activity. O-Cu_2O-A constitutes a plasmonic-activated electrochemical system: in-situ-formed Cu dendrites act as light absorbers to excite electron–hole pairs through LSPR, and Cu_2O nanostructures serve as active sites and hot-electron acceptors to facilitate the HER process.

The in-situ-grown Cu dendrites during HER introduce plasmonic effects into Cu_2O with optimally exposed crystal facets, tune the carrier density of the catalyst to match the energy levels of target reactions, improve interfacial charge transfer, and thereby further promote the electrocatalytic HER efficiency. This method can also be extended to other inexpensive plasmonic metals, such as Al and Mg, to expand the spectral range of light absorption and reduce costs, enabling more applications in electrocatalytic and photocatalytic devices.

Supporting Information

Supporting Information is available from the Wiley Online Library or from the author.

Acknowledgements

H.Z. acknowledges the Imperial College London and China Scholarship Council for the IC-CSC joint scholarship, EPSRC Centre for Doctoral Training in the Advanced Characterization of Materials (EP/L015277/1). The authors acknowledge the use of characterization facilities within the Harvey Flower Electron Microscopy Suite at the Department of Materials, Imperial College London. The authors acknowledge the computational resources provided by the Texas Advanced Computing Center and the National Energy Research Scientific Computing Center under the support of the Welch Foundation (F-1841).

Conflict of Interest

The authors declare no conflict of interest.

Data Availability Statement

The data that support the findings of this study are available from the corresponding author upon reasonable request.

Keywords

copper dendrites, copper oxide, engineered facets, hot-electron injection, hydrogen evolution

Received: June 14, 2023
Revised: August 29, 2023
Published online: September 12, 2023

[1] I. Roger, M. A. Shipman, M. D. Symes, *Nat. Rev. Chem.* **2017**, *1*, 0003.
[2] J. Mahmood, F. Li, S. Jung, M. Okyay, I. Ahmad, S. Kim, N. Park, H. Young, J. Baek, *Nat. Nanotechnol.* **2017**, *12*, 441.
[3] S. Y. Lee, H. Jung, N.-K. Kim, H. S. Oh, B. K. Min, Y. J. Hwang, *J. Am. Chem. Soc.* **2018**, *140*, 8681.
[4] C. Li, R. Guo, Z. Zhang, T. Wu, W. Pan, *Small* **2023**, *19*, 2207875.

© 2023 The Authors. Advanced Materials published by Wiley-VCH GmbH

15214095, 2023, 42, Downloaded from https://onlinelibrary.wiley.com/doi/10.1002/adma.202305742 by Test, Wiley Online Library on [27/10/2023]. See the Terms and Conditions (https://onlinelibrary.wiley.com/terms-and-conditions) on Wiley Online Library for rules of use; OA articles are governed by the applicable Creative Commons License

[5] H. Chen, Y. Ji, T. Fan, *Phys. Chem. Chem. Phys.* **2022**, *24*, 25347.
[6] H. Xu, J.-X. Feng, Y. Tong, G.-R. Li, *ACS Catal.* **2016**, *7*, 986.
[7] J. Zhao, P. D. Tran, Y. Chen, J. S. C. Loo, J. Barber, Z. J. Xu, *ACS Catal.* **2015**, *5*, 4115.
[8] M. Jahan, Z. Liu, K. P. Loh, *Adv. Funct. Mater.* **2013**, *23*, 5363.
[9] L. Zeng, X. Guo, C. He, C. Duan, *ACS Catal.* **2016**, *6*, 7935.
[10] Q. Jiang, C. Ji, D. J. Riley, F. Xie, *Nanomaterials.* **2019**, *9*, 1.
[11] H. Li, X. Zhang, D. R. MacFarlane, *Adv. Energy Mater.* **2015**, *5*, 1401077.
[12] D. S. Kim, Y. B. Kim, J. H. Choi, H. W. Suh, H. H. Lee, K. W. Lee, S. H. Jung, J. J. Kim, N. G. Deshpande, H. K. Cho, *Adv. Energy Mater.* **2021**, *11*, 2101905.
[13] Y. Gao, Q. Wu, X. Liang, Z. Wang, Z. Zheng, P. Wang, Y. Liu, Y. Dai, M. H. Whangbo, B. Huang, *Adv. Sci.* **2020**, *7*, 1902820.
[14] C. Kim, K. M. Cho, K. Park, J. Y. Kim, G. T. Yun, F. M. Toma, I. Gereige, H. T. Jung, *Adv. Funct. Mater.* **2021**, *31*, 2102142.
[15] B. Kumar, S. Saha, K. Ojha, A. K. Ganguli, *Mater. Res. Bull.* **2015**, *64*, 283.
[16] X. F. Zhang, Y. Zhang, H. D. Huang, J. N. Cai, K. N. Ding, S. Lin, *New J. Chem.* **2018**, *42*, 458.
[17] R. A. N. Khasanah, C. H. Lee, Y. C. Li, C. H. Chen, T. S. Lim, C. R. Wang, P. Y. Chang, H. S. Sheu, F. S. S. Chien, *ACS Appl. Energy Mater.* **2022**, *5*, 15326.
[18] M. Zhang, H. Xue, X. Han, Z. Zhang, Y. Jiang, Y. Deng, W. Hu, *J. Colloid Interface Sci.* **2023**, *650*, 284.
[19] P. Babar, A. Lokhande, H. Ho Shin, B. Pawar, M. G. Gang, S. Pawar, J. H. Kim, *Small* **2018**, *14*, 1702568.
[20] D. Li, J. Y. Shi, C. Li, *Small* **2018**, *14*, 1704179.
[21] H. Zhang, S. Geng, M. Ouyang, H. Yadegari, F. Xie, D. J. Riley, *Adv. Sci.* **2022**, *9*, 2200146.
[22] M. Kuang, P. Han, Q. Wang, J. Li, G. Zhang, *Adv. Funct. Mater.* **2016**, *26*, 8555.
[23] H. Zhang, Q. Jiang, J. H. L. Hadden, F. Xie, D. J. Riley, *Adv. Funct. Mater.* **2021**, *31*, 2008989.
[24] H. B. Zhang, P. F. An, W. Zhou, B. Y. Guan, P. Zhang, J. C. Dong, X. W. Lou, *Sci. Adv.* **2018**, *4*, 6657.
[25] H. Zhang, J. Diao, M. Ouyang, H. Yadegari, M. Mao, J. Wang, G. Henkelman, F. Xie, D. J. Riley, *Adv. Funct. Mater.* **2022**, *32*, 2205974.
[26] H. Tian, H. Tian, W. Yang, F. Zhang, W. Yang, Q. Zhang, Y. Wang, J. Liu, S. R. P. Silva, H. Liu, G. Wang, *Adv. Funct. Mater.* **2021**, *31*, 2101796.
[27] L. Xiao, G. Li, Z. Yang, K. Chen, R. Zhou, H. Liao, Q. Xu, J. Xu, *Adv. Funct. Mater.* **2021**, *31*, 2100982.
[28] X. Bao, Y. Gong, X. Zheng, J. Chen, S. Mao, Y. Wang, *J. Energy Chem.* **2020**, *51*, 272.
[29] T. R. Kuo, Y. C. Lee, H. L. Chou, M. G. Swathi, C. Y. Wei, C. Y. Wen, Y. H. Chang, X. Y. Pan, D. Y. Wang, *Chem. Mater.* **2019**, *31*, 3722.
[30] P. Christopher, H. Xin, A. Marimuthu, S. Linic, *Nat. Mater.* **2012**, *11*, 1044.
[31] C. Wang, X. G. Nie, Y. Shi, Y. Zhou, J. J. Xu, X. H. Xia, H. Y. Chen, *ACS Nano* **2017**, *11*, 5897.
[32] Z. Zheng, W. Xie, M. Li, Y. H. Ng, D. W. Wang, Y. Dai, B. Huang, R. Amala, *Nano Energy* **2017**, *41*, 233.
[33] H. Zhang, P. Li, H. Zhou, J. Xu, Q. Jiang, J. H. L. Hadden, Y. Wang, M. Wang, S. Chen, F. Xie, D. J. Riley, *Nano Energy* **2022**, *9*, 106968.
[34] C. Kim, B. L. Suh, H. Yun, J. Kim, H. Lee, *ACS Catal.* **2017**, *7*, 2294.
[35] Y. Shi, J. Wang, C. Wang, T. T. Zhai, W. J. Bao, J. J. Xu, X. H. Xia, H. Y. Chen, *J. Am. Chem. Soc.* **2015**, *137*, 7365.
[36] M. E. Aguirre, R. Zhou, A. J. Eugene, M. I. Guzman, M. A. Grela, *Appl. Catal. B* **2017**, *217*, 485.
[37] Y. Ma, L. Zhang, Z. Yan, B. Cheng, J. Yu, T. Liu, *Adv. Energy Mater.* **2022**, *12*, 2103820.
[38] Y.-T. Xu, Y. Guo, C. Li, X.-Y. Zhou, M. C. Tucker, X.-Z. Fu, R. Sun, C.-P. Wong, *Nano Energy* **2015**, *11*, 38.
[39] M. Moradzaman, G. Mul, *ACS Catal.* **2020**, *10*, 8049.
[40] D. Ren, Y. Deng, A. D. Handoko, C. S. Chen, S. Malkhandi, B. S. Yeo, *ACS Catal.* **2015**, *5*, 2814.
[41] L. Yu, X. Ba, M. Qiu, Y. Li, L. Shuai, W. Zhang, Z. Ren, Y. Yu, *Nano Energy* **2019**, *60*, 576.
[42] P. Dias, M. Schreier, S. D. Tilley, J. S. Luo, J. Azevedo, L. Andrade, D. Q. Bi, A. Hagfeldt, A. Mendes, M. Gratzel, M. T. Mayer, *Adv. Energy Mater.* **2015**, *5*, 1501537.
[43] Y. Yang, A. He, H. Li, Q. Zou, Z. Liu, C. Tao, J. Du, *ACS Catal.* **2022**, *12*, 12942.
[44] H. Yang, Y. W. Hu, J. J. Chen, M. S. Balogun, P. P. Fang, S. Zhang, J. Chen, Y. Tong, *Adv. Energy Mater.* **2019**, *9*, 1901396.
[45] T. Shinagawa, G. O. Larrazabal, A. J. Martin, F. Krumeich, J. Perez-Ramirez, *ACS Catal.* **2018**, *8*, 837.
[46] Y. Shang, L. Guo, *Adv. Sci.* **2015**, *2*, 1500140.
[47] Y. Pan, H. Li, J. Xiong, Y. Yu, H. Du, S. Li, Z. Wu, S. Li, J. Lai, L. Wang, *Appl. Catal. B* **2022**, *306*, 121111.
[48] Z. Liu, Y. Lu, L. Yuan, L. Ma, L. Zheng, J. Zhang, T. Hu, *Appl. Catal. B* **2016**, *188*, 189.
[49] H. Mistry, F. Behafarid, R. Reske, A. S. Varela, P. Strasser, B. R. Cuenya, *ACS Catal.* **2016**, *6*, 1075.
[50] G. Gan, X. Li, S. Fan, Z. Yin, L. Wang, G. Chen, *Nano Energy* **2021**, *80*, 105532.
[51] N. Cao, Z. Chen, K. Zang, J. Xu, J. Zhong, J. Luo, X. Xu, G. Zheng, *Nat. Commun.* **2019**, *10*, 2877.
[52] F. Huang, S. Xi, J. Song, S. Dou, X. Li, Y. Du, C. Diao, Z. J. Xu, X. Wang, *Nat. Commun.* **2021**, *12*, 3992.
[53] C. Choi, T. Cheng, M. Flores Espinosa, H. Fei, X. Duan, W. A. Goddard III, Y. Huang, *Adv. Mater.* **2019**, *31*, 1805405.
[54] Y. S. Zhou, F. L. Che, M. Liu, C. Q. Zou, Z. Q. Liang, P. De Luna, H. F. Yuan, J. Li, Z. Q. Wang, H. P. Xie, H. M. Li, P. N. Chen, E. Bladt, R. Quintero-Bermudez, T. K. Sham, S. Bals, J. Hofkens, D. Sinton, G. Chen, E. H. Sargent, *Nat. Chem.* **2018**, *10*, 974.
[55] Y. Mun, S. Lee, A. Cho, S. Kim, J. W. Han, J. Lee, *Appl. Catal. B* **2019**, *246*, 82.
[56] H. Zhang, S. Geng, M. Ouyang, M. Mao, F. Xie, D. J. Riley, *Small* **2021**, *17*, 2106391.
[57] S. Meng, C. Chen, X. Gu, H. Wu, Q. Meng, J. Zhang, S. Chen, X. Fu, D. Liu, W. Lei, *Appl. Catal. B* **2021**, *285*, 119789.
[58] H. Zhang, P. Li, S. Chen, F. Xie, D. J. Riley, *Adv. Funct. Mater.* **2021**, *31*, 2106835.
[59] X. Wang, X. Zhao, D. Zhang, G. Li, H. Li, *Appl. Catal. B* **2018**, *228*, 47.
[60] S. Roy, M. Miller, J. Warnan, J. J. Leung, C. D. Sahm, E. Reisner, *ACS Catal.* **2021**, *11*, 1868.
[61] H. Zhang, Y. Li, J. Wang, N. Wu, H. Sheng, C. Chen, J. Zhao, *Appl. Catal. B* **2021**, *284*, 119692.
[62] L. Zheng, F. Teng, X. Ye, H. Zheng, X. Fang, *Adv. Energy Mater.* **2020**, *10*, 1902355.
[63] Z. Zhang, L. Liu, W.-H. Fang, R. Long, M. V. Tokina, O. V. Prezhdo, *Chem* **2018**, *4*, 1112.
[64] Y. Liu, Z. Jiang, J. Jia, J. Robertson, Y. Guo, *Appl. Surf. Sci.* **2023**, *611*, 155674.
[65] Q. Zheng, W. A. Saidi, Y. Xie, Z. Lan, O. V. Prezhdo, H. Petek, J. Zhao, *Nano Lett.* **2017**, *17*, 6435.
[66] H. Guo, W. Chu, O. V. Prezhdo, Q. Zheng, J. Zhao, *J. Phys. Chem. Lett.* **2021**, *12*, 3960.

© 2023 The Authors. Advanced Materials published by Wiley-VCH GmbH

15214095, 2023, 42, Downloaded from https://onlinelibrary.wiley.com/doi/10.1002/adma.202305742 by Test, Wiley Online Library on [27/10/2023]. See the Terms and Conditions (https://onlinelibrary.wiley.com/terms-and-conditions) on Wiley Online Library for rules of use; OA articles are governed by the applicable Creative Commons License